NANOENERGETICS AND HIGH HYDROGEN CONTENT MATERIALS FOR SPACE PROPULSION

Steven F. Son, Vigor Yang, and Richard A. Yetter

2012 Air Force Office of Scientific Research (AFOSR)
Space Propulsion and Power Contractors Meeting
September 10-14, 2012
Arlington, VA

Abstract

Progress in the past year has occurred in the following areas: 1) understanding the role of pH and rheology on Al/water combustion, 2) encapsulation of nanoparticles in crystals for propellants, 3) disrupting ignition of aluminum with fluorocarbon inclusions, 4) the combustion of micron aluminum with hydrogen peroxide, and high speed PLIF applied to composite propellants, 5) the thermochemical behavior of Ni-coated Al particles, 6) the effects of particle size on melting, diffusion, and reactions, 7) the pyrophoricity of nano-aluminum particles, 8) the thermal decomposition and high temperature oxidation of ammonia borane (NH_3BH_3), particularly as an energetic fuel/additive, and 9) investigations of solid oxidizer and gaseous fuel combustion performance using counterflow burners and reverse hybrid motors. Each of these topics are described in more detail below.

The Dependence of Nano-Aluminum and Water Propellant Combustion on pH and Rheology

Over the past few years, the combustion of nano-aluminum/water (nAl/H_2O) propellants has been widely reported, but further progress has been slowed for the following reason: the loosely correlated trends in combustion data are insufficient in guiding further research efforts, and they cannot be used to significantly improve the Isp observed in static rocket motor tests. It was previously found that different mixing techniques (hand, planetary and resonant mixers, duration and temperature), or equivalence ratio gave rise to different burning rates, but the influence of pH and rheology on nAl/H_2O propellants was not considered. We find that the effects of pH on nAl/H_2O propellants are profound, and correlate well with viscosity, low-pressure deflagration limits, burning rate exponents, and rocket motor performance. Our findings suggest that coagulation can influence the pressure exponent over a wide range of values (0.34-0.68). For particle diameters < 1 μm, dispersion during mixing is affected more by electrostatic repulsion from charged ions than from mechanical agitation, and this is reflected through zeta potential and viscosity measurements at different pH levels. Additionally, we observe that pH has an influence on nAl/H_2O reaction kinetics during ignition, as the propellant transitions from low temperature oxidation to high temperature combustion.

Preparation and Characterization of Energetic Crystals with Nanoparticle Inclusions

In this work, we have reported on the preparation and characterization of energetic crystals with nanoparticle inclusions. We focus on the nanosized iron (III) oxide-ammonium perchlorate system, generated using an ethyl acetate-acetone antisolvent:solvent system. It was shown that capture is dependent on antisolvent-to-solvent ratio; increased quantities of antisolvent lead to faster growth rates, smaller crystals, and improved capture. Additionally, the

crystal habit formation is modified by the addition of nanoparticles, resulting in highly uniform quadrate crystal structures. In addition, results with nanoaluminum-ammonium perchlorate and nanoaluminum-cyclotrimethylenetrinitramine (RDX) systems have shown similar capture behavior.

Disruption of ignition barriers in micron aluminum with selective inclusion of polytetrafluoroethylene

Micrometer aluminum is ubiquitous in energetic materials; however, performance of propellants, explosives and pyrotechnics could be significantly improved if ignition barriers could be disrupted. We have reported morphological, thermal, and chemical characterization of fuel rich aluminum-polytetrafluoroethylene (PTFE) (70-30 wt.%) reactive particles formed via high and low energy milling. Average particle sizes range from 15-78 micron and specific surfaces areas range from ~2-7 m^2/g. Scanning electron microscopy and energy dispersive spectroscopy reveal uniform distribution of the PTFE, providing nanoscale mixing within particles. The heat of combustion was found to be 23.4 kJ/g, though a slight decrease (0.9 kJ) results from extended high energy milling due to AlF_3 formation. Differential scanning calorimetry (DSC) in argon shows a strong, exothermic pre-ignition reaction (PIR) near 450 °C and a second, more dominant exotherm around 540 °C. Scans in O_2-Ar indicate that, unlike physical mixtures, more complete reaction occurs and at higher heating rates, the reaction onset is drastically reduced (~470 °C). Simple flame tests reveal that these altered Al-PTFE particles light readily, unlike micron sized Al. These particles may be useful for reactive liners, thermobaric explosives, and pyrolant formulations. In particular, the altered ignitability, large particle size and relatively low specific surface area of these fuel rich particles make them an interesting replacement for aluminum in solid propellants.

High speed planar laser induced fluorescence (PLIF) of composite propellants

The self deflagration of a bimodal ammonium perchlorate (AP) and hydroxyl-terminated polybutadiene (HTPB) propellant was studied using high speed (5 kHz) planar laser induced fluorescence (PLIF) for the first time. The qualitative OH concentration was characterized near the surface. In addition to OH, it was found that the larger AP particles can be imaged as they fluoresce when exposed to laser radiation centered at 283.2 nm. Single AP particle ignition delay, lifetime, and flame height are determined as a function of particle diameter over a range from 100 to 500 μm at 1 atm within the burning sample. High speed visible imaging was also completed to confirm the trends seen during PLIF experiments, although the fluoresced particles have much improved contrast. Ignition delay times and single particle burn times were compared with a model proposed by Shannon and Peterson. The measured final diffusion flame height above a regressing AP crystal was compared with an expression used by the Beckstead, Derr, and Price (BDP) model. It was found that the AP/HTPB propellant flame structure varies significantly with particle size, even at 1 atm. The models are found to adequately predict the observed trends, but do not capture the interaction of adjacent particles. The interaction of particles close to each other appears to affect behavior significantly and more detailed modeling is needed. It is shown that 5 kHz OH PLIF can be a valuable tool to characterize AP composite propellant combustion.

The catalytic effect of iron (III) oxide (Fe_2O_3) and copper (II) oxide (CuO) on an ammonium perchlorate (AP) and hydroxyl-terminated polybutadiene (HTPB) propellant was studied also using High speed (5 kHz) planar laser induced fluorescence (PLIF). Visible

microscopic imaging of the surface was carried out in an effort to determine the mechanisms that account for the effect of catalysts. Diffusion flame lengths, crystal burn times, and ignition delay times for single AP crystals were measured during deflagration of catalyzed propellants at 1 atm. A long distance microscopic lens was also used to image AP crystal behavior in the presence of the catalysts. General trends observed on the surface are discussed. The addition of a transition metal oxide (TMO) catalyst greatly reduces the ignition delay times of the AP crystals while not significantly altering the coarse AP crystal burn times. The diffusion flame length was found to increase proportionally with the propellant's burning rate. The findings of this experimental study provide evidence that the fine AP/binder mixture is affected most by the catalyst rather than the coarse AP at 1 atm.

Examination of the surface behavior and flame structure of a bimodal ammonium perchlorate (AP) composite propellant at elevated pressure was also performed using PLIF from 1-12 atm and visible surface imaging spanning 1-20 atm. The dynamics of the combustion of single, coarse AP crystals were resolved using these techniques. It was found that the ignition delay time for individual AP crystals contributed significant to the particle lifetime only at pressures below about 6 atm. In situ AP crystal burning rates were found to be higher than rates reported for pure AP deflagration studies. The flame structure was studied by exciting OH molecules in the gas phase. Two types of diffusion flames were observed above the composite propellant: jet-like flames and v-shaped, inverted, overventilated, flames (IOF) lifted off the surface. While jet-like diffusion flames have been imaged and simulated by models, the lifted IOFs have not been previously reported or predicted. The causes for the observed flame structures are explained by drawing on an understanding of the surface topography and disparities in the burning rates of the fuel and oxidizer.

The thermochemical behavior of Ni-coated Al particles

Aluminum particles are extensively used in many propulsion and energy-conversion applications due to their favorable energetic properties [1]. They are covered by an amorphous oxide layer, which is typically 0.5-4 nm thick [2]. Particles with diameter greater than 100 μm ignite only upon melting of the oxide layer at 2350 K [3]. This results in a long ignition delay and slow rates of energy release. Nano-sized aluminum particles can ignite at the melting temperature of the core, 933 K [3]. The oxide layer, however, occupies a significant portion of the particle mass at nano-scales. For example, a 38 nm aluminum particle has ~47.5 wt. % oxide [4]. It is, thus, desirable to replace the oxide layer with other favorable metallic coatings such as nickel [5]. Nickel atoms can participate in inter-metallic reactions with aluminum atoms and oxidizing reactions with oxygen molecules. This reduces the ignition delay and increases the energy content of the particle. For example, the ignition temperature of a 2.38 mm aluminum particle in air decreases from 2350 to 1313 K, when the oxide layer is replaced with a nickel coating [6].

Molecular dynamics (MD) simulations were performed to investigate the thermochemical behavior of nickel-coated aluminum particles. The core diameter was varied in the range of 3-12 nm and the shell thicknesses of 0.5, 1, 2, and 3 nm were considered. Special attention was placed to quantify the effect of the nickel shell on melting point of the core and to analyze the effect of atoms diffuse outwards into the shell and nickel atoms core size and shell thickness on melting, core diameter and shell thickness on melting, diffusion, and inter-metallic reactions. Both isobaric-isothermal (NPT) and isochoric-isoenergetic (NVE) ensembles were employed. The equations of motion in different ensembles, generated using the Euler-Lagrange method, were

numerically integrated using a fifth-order predictor-corrector algorithm [7]. The time step was chosen as 1 fs because the time scale of vibration of atoms is of the same order. An optimum heating rate of 10^{-2} K/fs was chosen based on the results of a parametric study. Figure 1 shows the important thermo-chemical processes occurring in the particle over a temperature range of 800-2400 K. At 800 K, both the core and the shell are in solid state. Upon core melting, the aluminum atoms diffuse outwards into the shell and nickel atoms diffuse inwards into the core to transform the aluminum-nickel particle into a homogeneous alloyed particle through inter-metallic reactions. The diffusion processes are caused by the presence of the radial concentration gradient. They are predominant upon melting owing to the higher mobility of the melted atoms. Figure 2 shows the effect of core size on the melting point of the core. It increases from 900 to 1010 K, when the core diameter increases from 3 to 12 nm. This is due to the decrease in the percentage of the interfacial aluminum atoms with increasing core size. In all the cases, the presence of the nickel shell increases the melting point of the core. In particular, the melting point of the core is higher than the asymptotic melting point of the nascent particle (883 K) and lower than the structural melting point of the surface-free bulk aluminum (1060 K). The nickel shell imposes mechanical constraint to the motion of the interfacial aluminum atoms, thereby increasing the core melting point. The chemical heat release due to inter-metallic reactions results in particle self-heating from the initial temperature to a much higher value at equilibrium.

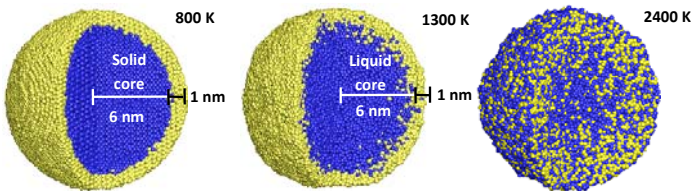

Fig. 1. Snapshots of 14 nm particle (1 nm shell) showing melting and diffusion processes

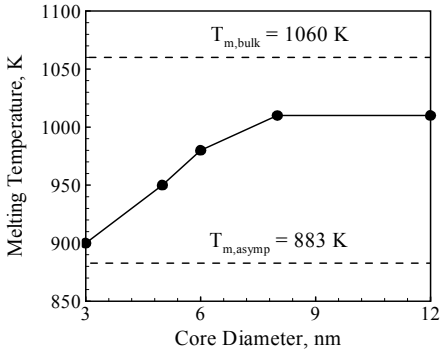

Fig. 2. Core melting point vs. core diameter (δ_s=1 nm)

Effects of particle size on melting, diffusion, and reactions

Simulations in NVE ensemble were performed to ascertain the effect of core size on the equilibrium temperature of the particle upon completion of the inter-metallic reactions. The initial position and velocities of the atoms are those obtained from the heating simulation in NPT ensemble at the onset temperature of the inter-metallic reactions. The outcome of the calculations is shown in Fig. 3. The equilibrium temperature increases with increasing core diameter, since a larger core has more number of aluminum atoms to react with nickel atoms. The shell thickness was varied in the range of 0.5-2 nm to ascertain the influence of the shell on the diffusion patterns of

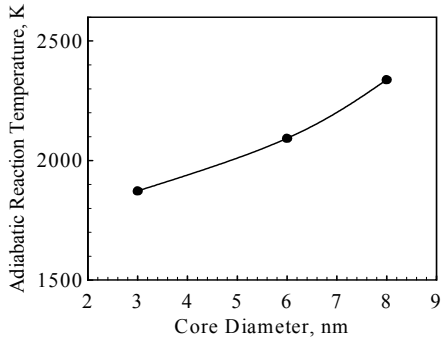

Fig. 3. Adiabatic reaction temperature vs. core size for a 1 nm thick shell

aluminum atoms for a fixed core diameter of 3 nm. Figure 4 shows the core radius as a function of temperature for different values of shell thickness. For a 0.5 nm shell, the core radius increases significantly upon melting of the core at 800 K. The core atoms, however, begin to diffuse out only at 1400 and 1600 K for shell thickness of 1 and 2 nm, respectively. This is related to the melting of the shell, since the shell melts at a temperature greater than that of the core. Diffusion is facilitated for thinner shells. A series of MD simulations was performed to determine the shell melting point as a function of its thickness for a fixed core diameter of 3 nm. Figure 5 shows result. The shell melting point increases from 1350 to 1580 K, when the thickness increases from 1 to 3 nm. Note that these values are lower than the melting point of bulk nickel, 1728 K. The calculated melting points explain the observed increase in the core radius at 1400 and 1600 K for shell thickness of 1 and 2 nm, respectively. The thickness of the shell, thus, has profound impact on the thermo-chemical behavior of nickel coated aluminum particles.

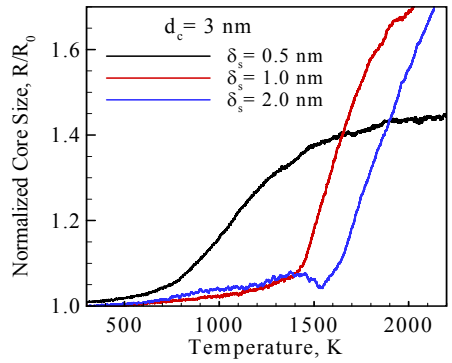

Fig. 4. Core radius vs. temperature for shell thickness of 0.5, 1 and 2 nm

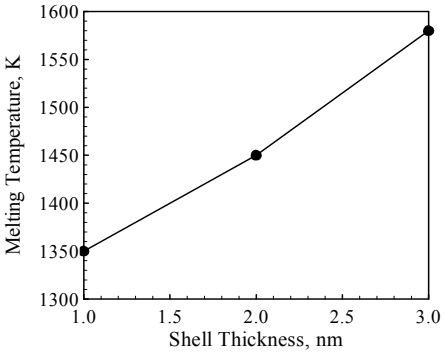

Fig. 5. Shell melting temperature vs. thickness for a core diameter of 3 nm

Pyrophoricity of nano-aluminum particles

At nano-scales, the enhanced reactivity of the particle poses significant safety hazards. If the diameter of the particle is decreased below a critical value, the particle could ignite when exposed to an oxidizing gas at room temperature, a phenomenon known as pyrophoricity [8]. It is a major safety issue during particle manufacture and storage. It can also be employed for useful applications like decoy flare for defending heat-seeking missiles [9]. Reliable measurements or predictions of the critical particle size for both nascent and passivated aluminum particles are of paramount interest. Puri and Yang [10] performed an unsteady energy balance analysis to study the pyrophoricity of nano-aluminum particles. The model considered plane Mott-Cabrera oxidation kinetics and size-dependence of physiochemical properties. The calculated critical particle size was 20 nm. A similar analysis was performed by Mohan et al. [11], but employed bulk physiochemical properties along with particle version of the Mott-Cabrera model. The calculated critical particle size was 68 nm. In this work, the size-dependence of physiochemical properties and the Mott-Cabrera model applicable for spherical particles are considered. The specific heat was calculated at mean temperature. The density of the oxide layer was taken to be that of the amorphous phase, 3.05 g/cm^3. Both free-molecular and radiation heat

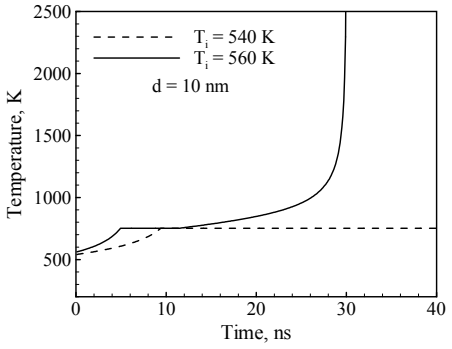

Fig. 6. Particle temperature as a function of time for core diameter of 10 nm and shell thickness of 0.3 nm

transfer were considered. Two sets of calculations were performed. In the first calculation, the minimum temperature necessary for ignition of particles with 0.3 nm thick oxide layer was calculated using the numerical model. Figure 6 shows the particle temperature as a function of time for a core diameter of 10 nm and shell thickness of 0.3 nm. For an initial temperature of 540 K, the rate of chemical heat-release is lower than that of heat loss to the ambient environment. As a result, temperature runaway is not observed. The temperature increases sharply after a time period of 25 ns, when the initial temperature is chosen as 560 K. This phenomenon was observed for all temperatures greater than 560 K. For a particle with a 10 nm core, the minimum ignition temperature can be taken as 560 K. A similar analysis was performed for different particle sizes and the minimum ignition temperature was determined as a function of the particle size. In the second calculation, thermodynamic analysis was performed to calculate the particle temperature upon growth of 0.3 nm thick oxide layer. If this value is higher than the minimum ignition temperature, the corresponding particle is considered to be pyrophoric. Figure 7 shows the comparison of the two calculations. The thermodynamic analysis indicates that the particle temperature decreases with increasing particle size, since more energy is spent to heat a larger particle. The numerical analysis, on the other hand, suggests that the minimum ignition temperature increases with the particle size, since the rate of heat loss to the oxidizing gas is proportional to the particle surface area. These two curves interest at the critical particle size of 37 nm, which is lower than the value of 68 nm predicted in Ref. [11] and higher than the value of 20 nm predicted in Ref. [10]. This underlines the important effect of size-dependent properties and accurate evaluation of physiochemical properties in the model results. A similar analysis indicates that particles smaller than 3.8 nm are pyrophoric, when the oxide layer thickness is 0.3 nm. When the oxide thickness is increased beyond 0.3 nm, particles become non-pyrophoric.

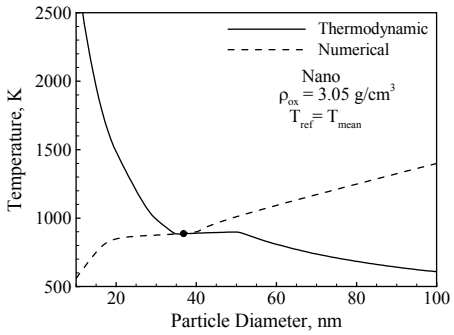

Fig. 7. Particle temperature after the growth of 0.3 nm oxide layer and the minimum temperature for ignition

Thermal decomposition and high temperature oxidation studies of ammonia borane (NH_3BH_3) as an energetic fuel/additive (in collaboration with Professor Stefan Thynell and Professor Adri van Duin at PSU)

Ammonia borane is a hydrogen rich compound recently studied as a means for high density hydrogen storage. Thermochemical calculations of ammonia borane (AB, H_3NBH_3), which has a hydrogen content of 19.6% by weight, indicate that it has the potential to boost specific impulse in chemical propulsion applications due to its high hydrogen content and the moderate exothermicity of decomposition. Research to date on AB decomposition has focused on relatively slow heating rates. These studies have shown that the mass lost due to decomposition increases with increasing heating rate. This trend has been confirmed in this work, as mass loss continues to increase up to 50 K/min, the limit of most TGA/DSC instruments. In our current research effort, confined rapid thermolysis was used to examine the decomposition of AB under isothermal conditions. Fourier transform infrared (FTIR) spectroscopy and time-of-flight mass spectrometry (ToF-MS) were employed to identify the gaseous products, which include H_2, NH_3, H_2NBH_2, and c-$N_3B_3H_6$. The decomposition resulted in significant condensed-phase products as well, which were pressed into a KBr pellet and

examined with FTIR spectroscopy. FTIR transmission spectra of the condensed-phase products with several heating durations show the disappearance of absorption bands of AB and appearance of bands attributed to polymeric species. Condensable gas-phase products were also collected from the stream of decomposition products, and FTIR spectroscopy showed they have absorption bands similar to the polymeric species, indicating that the H_2NBH_2 will readily condense out of the gas-phase products and polymerize at low temperatures.

In order to investigate the reaction mechanism associated with the decomposition and oxidation of AB at an atomistic scale, a reactive force field (ReaxFF) has been developed for use in molecular dynamics (MD) simulations. The ReaxFF parameters have been derived directly from quantum mechanical data (QM). NVT-MD simulations of single and poly-molecular AB thermolysis were conducted in order to validate the force field. The release of the first equivalent H_2 is a unimolecular reaction, and MD simulations show an activation energy of 26.36 kcal mol^{-1}, which is in good agreement with experimental results. The release of the second H_2 is also a uni-molecular reaction, however, the release of a third H_2 requires the formation of a B-N polymer. Similar simulations were conducted with a boron and oxygen system, since the oxidation of boron will be an integral step in AB combustion, and show good agreement with the established mechanism for this system. At low temperatures, boron atoms agglomerate into a cluster, which is oxidized at higher temperatures, eventually forming condensed and gas phase boron-oxide-species. These MD results provide confidence that ReaxFF can properly model the oxidation of AB and provide mechanistic insight into the AB dehydrogation and combustion reactions.

The chemical kinetics of ammonia borane oxidation have been studied using molecular dynamics simulations performed with a ReaxFF reactive force field, which in turn, is based on *ab initio* data. This approach allows for the development of a continuum model of ammonia borane oxidation, which after refinement can be used to model fundamental experiments, without any prior experimental data. The results of molecular dynamics simulations elucidate the pertinent chemical pathways and intermediate species needed to define the elementary reactions of a simple chemical kinetic mechanism. These simulations show that the gas phase ammonia borane molecule first undergoes two hydrogen elimination steps. Subsequently, the H_2 reacts with the O_2 in the system, while the boron side of the remaining HNBH molecule is attacked by oxygen, eventually leading to the cleavage of the B-N bond and the formation of the equilibrium products H_2O, HOBO, and N_2. Due to the high densities used in these simulations, H_2O_2 and HO_2 are favored as intermediates over OH. Since H_2O_2 and HO_2 are not very effective at hydrogen abstractions, the hydrogen elimination reactions are favored. Density functional theory calculations were used to calculate unknown thermochemical properties, and simple collision theory was used to estimate reaction rate constants. The resulting continuum kinetic model, comprised of 50 species, 52 new reactions, 200 total reactions, was used to perform simple closed reactor, constant pressure and energy calculations in CHEMKIN, the results of which are consistent with the observations made at the atomistic level in the molecular dynamics simulations. This work demonstrates how a combination between *ab initio* calculations, molecular dynamics and thermodynamics equilibrium calculations can be employed to elucidate complex combustion reaction kinetics.

Investigation of solid oxidizer and gaseous fuel combustion performance using counterflow burner and reverse hybrid motor

Pressurized counterflow and static-fired motor studies were conducted to explore the possibility of a reverse hybrid system, having a solid oxidizer and gaseous fuel. Theoretical performance analysis indicates such a system may yield specific impulse and density specific impulse similar to composite solid propellants, yet with the added capability to throttle, shut down, and restart firings. Pressurized counterflow studies conducted using pressed ammonium perchlorate pellets and gaseous ethylene show three pressure dependent combustion regimes. At pressures below 1 MPa, ammonium perchlorate decomposition is controlled by heat transfer from the resulting fuel/oxidizer diffusion flame, exhibiting a weak dependence on flame strain rate and burning rates between 0.01 to 0.05 cm/s. As pressure increases, the monopropellant flame moves closer to the oxidizer surface until the pressure reaches the self-decomposition limit near 3 MPa , which indicates that when the monopropellant flame dominates the diffusion flame. Further increasing the pressure yields burning rates between 0.4 to 0.7 cm/s, which are consistent with the literature, and exhibit little strain rate dependence for the range of flow conditions tested. Similar studies conducted with methane yielded no variation in burning rates, suggesting independence of fuel type. Lab-scale static motor firings focused on the mid- to high-pressure combustion regime, examining ignition, repeatability, and system performance. Results indicate that combustion is highly dependent on the initial pressure of the motor, producing a fast burn with initial pressures of 4.45 and 2.20 MPa, while behaving like a gas generator at a lower initial pressure of 1.14 MPa.

References

[1] E.W. Price, R.K. Sigman, Solid Propellant Chemistry, Combustion, and Motor Interior Ballistics, V. Yang, T.B. Brill, W.Z. Ren, AIAA Progress in Astronautics and Aeronautics, 185, 2000, 663-687.
[2] M.A. Trunov, M. Schoenitz, E.L. Dreizin, Combust. Theory Model. 10 (4) (2006) 604-623.
[3] Y. Huang, G. A. Risha, V. Yang, and R. A. Yetter, Combust. Flame 156 (2009) 5-13.
[4] G.A. Risha, S.F. Son, R.A. Yetter, V. Yang, Proc. Combust. Inst. 31 (2007) 2029-2036.
[5] T.J. Foley, C.E. Johnson, K.T. Higa, Chem. Mater. 17 (2005) 4086-4091.
[6] E. Shafirovich, A. Mukasyan, L. Thiers, A. Varma, B. Legrand, C. Chauveau, I. Gokalp. Combust. Sci. Tech. 174 (2002) 125-140.
[7] P. Puri, V. Yang, J. Phys. Chem. C 111 (2007) 11776-11783.
[8] I. Glassman, P. Papas, K. Brezinsky, Combust. Sci. and Technol. 83 (1992) 161-165.
[9] A. L. Baldi, Patent 5028385, http://www.freepatentsonline.com/5028385.html, July 1991.
[10] P. Puri, Ph.D. Thesis, The Pennsylvania State University, 2008.
[11] S. Mohan, A. Ermoline, E.L. Dreizin, J. Nanoparticle Research 14 (2012) 723-729